NeuroImage 232 (2021) 117895

Contents lists available at ScienceDirect

NeuroImage

journal homepage: www.elsevier.com/locate/neuroimage

Temporal trajectory of brain tissue property changes induced by electroconvulsive therapy

L. Gyger[a,b], C. Ramponi[b], J.F. Mall[c], K. Swierkosz-Lenart[c], D. Stoyanov[d], A. Lutti[b], A. von Gunten[c], F. Kherif[b,#], B. Draganski[b,e,#,*]

[a] Laboratoire de Psychologie et NeuroCognition, Université Grenoble Alpes, Grenoble, France
[b] LREN, Dept. of clinical neurosciences, Lausanne University Hospital and University of Lausanne, Lausanne, Switzerland
[c] Old Age Psychiatry service - Department of Psychiatry, Lausanne University Hospital and University of Lausanne, Lausanne, Switzerland
[d] Department of Psychiatry and Medical Psychology & Research Institute, Medical University Plovdiv, Bulgaria
[e] Neurology Department, Max Planck Institute for Human Cognitive and Brain Sciences, Leipzig, Germany

ARTICLE INFO

Keywords:
Longitudinal MRI
Electroconvulsive therapy
Voxel-based morphometry
Voxel-based quantification
Major depression
Hippocampus

ABSTRACT

Background: After more than eight decades of electroconvulsive therapy (ECT) for pharmaco-resistant depression, the mechanisms governing its anti-depressant effects remain poorly understood. Computational anatomy studies using longitudinal T1-weighted magnetic resonance imaging (MRI) data have demonstrated ECT effects on hippocampus volume and cortical thickness, but they lack the interpretational specificity about underlying neurobiological processes.

Methods: We sought to fill in the gap of knowledge by acquiring quantitative MRI indicative for brain's myelin, iron and tissue water content at multiple time-points before, during and after ECT treatment. We adapted established tools for longitudinal spatial registration of MRI data to the relaxometry-based multi-parameter maps aiming to preserve the initial total signal amount and introduced a dedicated multivariate analytical framework.

Results: The whole-brain voxel-based analysis based on a multivariate general linear model showed that there is no brain tissue oedema contributing to the predicted ECT-induced hippocampus volume increase neither in the short, nor in the long-term observations. Improvements in depression symptom severity over time were associated with changes in both volume estimates and brain tissue properties expanding beyond mesial temporal lobe structures to anterior cingulate cortex, precuneus and striatum.

Conclusion: The obtained results stemming from multi-contrast MRI quantitative data provided a fingerprint of ECT-induced brain tissue changes over time that are contrasted against the background of established morphometry findings. The introduced data processing and statistical testing algorithms provided a reliable analytical framework for longitudinal multi-parameter brain maps. The results, particularly the evidence of lack of ECT impact on brain tissue water, should be considered preliminary considering the small sample size of the study.

1. Introduction

Major depressive disorder (MDD) affects estimated 300 million individuals worldwide and is the second main contributor to the Years Lived with Disability (DALY) (James et al., 2018). Despite the existing therapeutic armament, a third of patients are pharmaco-resistant and require electroconvulsive therapy (ECT), which is established as effective and rapid non-pharmacological treatment with remission rates between 40 and 70% (The UK ECT REVIEW GROUP 2003). The existing controversies about ECT's application in the clinical routine are partially due to ongoing debate about its mechanisms of action and impact on brain structure and function (Read et al., 2019).

Pre-clinical studies showed that ECT-induced neurogenesis in the hippocampus might explain its beneficial treatment effects (Ueno et al., 2019). Computational anatomy investigations using MRI in patients with depression, provided strong empirical evidence for ECT-induced changes in brain anatomy, perfusion and function, whilst consistently reporting hippocampal volume increases (Argyelan et al., 2019, Dukart et al., 2014, Joshi et al., 2016, Leaver et al., 2018, Nuninga et al., 2020, Oltedal et al., 2018, Ousdal et al., 2020, Takamiya et al., 2019 Sep, Wade et al., 2017). Along the same lines, recent investigations with ultra-high field 7T MRI or dedicated atlas-based parcellation of the hip-

* Corresponding author.
E-mail address: bogdan.draganski@chuv.ch (B. Draganski).
# Equal contribution.

https://doi.org/10.1016/j.neuroimage.2021.117895
Received 28 October 2020; Received in revised form 31 December 2020; Accepted 16 February 2021
Available online 19 February 2021

pocampus corroborated the idea of ECT-induced neurogenesis by localising the observed morphometry findings to the dentate gyrus of the hippocampus (Nuninga et al., 2020). However, these studies were unable to provide a straightforward neurobiological interpretation of the obtained morphometry results mainly because they relied on T1-weighted MRI protocols that cannot differentiate between the main tissue property contributors to MR contrast. This limitation of the T1-weighted MRI protocols can result in "spurious" interpretation of morphometric findings, as demonstrated in the case of brain maturation (Natu et al., 2019) and ageing (Lorio et al., 2016).

From another perspective, observations of abnormal diffusion MRI signal in the mesial temporal lobe of patients with status epilepticus, allow for speculations that the observed ECT-induced hippocampus volume changes are related to oedema (Kim et al., 2001, Righini et al., 1994, Szabo et al., 2005). Supporting this assumption, early nuclear magnetic resonance studies reported increased T1-relaxation time immediately after ECT (Mander et al., 1987) (Scott et al., 1990). The lack of T2-relaxation time differences (Kunigiri et al., 2007) is a weak argument against the hypothesis of ECT-induced oedema, given that T2-relaxation is a composite measure not entirely linked to water content Tofts (2004). Similarly, the reported ECT-induced changes in mean diffusivity contrasted against stable apparent diffusion coefficient measurements in the hippocampus (Szabo et al., 2007) cannot rule out an ECT-induced oedema given they are influenced by the proportion of water in intra- vs extracellular compartments and do not provide an absolute measure of water content. Most recently, a study combining brain perfusion measurements with tensor-based index of mean diffusivity (MD) reported ECT-induced MD changes contrasted to the absence of perfusion or intravoxel incoherent motion that were interpreted as lack of evidence for angiogenesis or oedema (Nuninga et al., 2020).

Quantitative MRI (qMRI) based on biophysical models offers detailed insight in brain's tissue properties by providing measurements of magnetisation transfer (MT) saturation, longitudinal relaxation rate (R1=1/T1), effective transverse relaxation rate ($R2^*=1/T2^*$) and proton density (PD) (Weiskopf et al., 2015). MT and particularly the MT saturation are established as specific marker of myelin content (Laule et al., 2007). Similarly, the interactions of water with the molecular components of the myelin sheaths relate to changes in T1, respectively R1 Koenig (1991). Paramagnetic iron induces local magnetic field perturbations associated with enhanced $R2^*$ relaxation (Stüber et al., 2014). PD reflects the MR-visible water content and its increase is indicative for loss of MR-invisible macromolecules (Mezer et al., 2013). qMRI addresses the shortcomings of previous research by assessing the contribution of measurable brain tissue properties to MR contrast, thus offering a straightforward neurobiological interpretation of processes underlying brain maturation, ageing and brain plasticity (Natu et al., 2019, Lorio et al., 2016). The quantitative character of the measurements with low inter-scanner variability (Weiskopf et al., 2013) and bias-free associated signal stability over time (Gracien et al., 2020) renders qMRI an optimal technique for longitudinal studies (Weiskopf et al., 2015).

Longitudinal qMRI studies face significant challenges regarding the choice and implementation of appropriate spatial and statistical modelling. Statistical modelling challenges stem from not acknowledging the doubly multivariate nature of these data with multiple time points and multiple contrasts. In this context, the statistical design is even more complex than a repeated measures issue. Previous multi-contrast MRI studies used simpler models fitting each contrast separately with one univariate General Linear Model (GLM) (Stefani et al., 2019). This strategy is known to inflate the type I error rate and does not model the relationship between dependent variables Fox (2015). The use of multivariate statistics allows for assessing how a combination of dependent variables reflects an effect of interest, and thus provides more information than the univariate GLM approach (McFarquhar et al., 2016, Stoyanov et al., 2019, Zufferey et al., 2017, Kherif et al., 2002 Aug 1). The recently proposed implementation of multivariate GLM for neuroimaging data (McFarquhar et al., 2016), facilitates the modelling of either multi-contrast datasets or repeated measures datasets, but do not handle the case of datasets that have both characteristics. Spatial modelling challenges have rarely been considered given the sparsity of qMRI studies with multiple acquisition time points (Natu et al., 2019, Ziegler et al., 2019). Spatial registration of longitudinal multi-parameter MRI data also require special attention as the linear and non-linear registration methods at hand can have a profound effect on the final results with different statistical outcomes.

To address limitations in spatial and statistical modelling of previous research, we introduce a whole-brain voxel-based mass-multivariate analytical approach in the framework of SPM12 that allows optimal modelling of multi-contrast and repeatedly measured data. We applied this strategy to our longitudinal qMRI study to allow the statistical testing of spatially aligned temporal trajectories of ECT-induced brain anatomy changes. The main question was to investaigate the association between ECT-related hippocampus volume increase and tissue water content changes. We additionally assess the clinical utility of the approach by testing the relationship between the multivariate latent variables of brain tissue microstructure and the clinical outcomes.

2. Materials and methods

2.1. Participants and study design

We recruited 9 patients (4 female, mean age 51.5 ± 11.4 years old) with current major depressive episode previewed for ECT treatment according to best clinical practice criteria. 5 patients had a diagnosis of major depressive disorder, 3 - bipolar disorder and 1 – schizo-affective disorder. A board-certified psychiatrist confirmed the diagnosis following the Diagnostic and Statistical Manual of Mental Disorders IV-TR American Psychiatric Association (2000). We tested symptom severity using the French version of the Montgomery-Åsberg Depression Rating Scale (MADRS, Montgomery and Åsberg (1979)) and defined ECT response as more than 50 % reduction of the MADRS score at baseline. Remission was concluded when the MADRS score was below or equal to 9 (Zimmerman et al., 2004). The local Ethics Committee approved the study and participants gave their written informed consent before participation.

We acquired neuroimaging data and symptom severity scores at four time points (see Fig. 1). The initial time point (t0) was before the start of ECT treatment, the second time point (t1) was during the first week of treatment after the first effective session of ECT. The third time point (t2) was two months after the start of ECT treatment corresponding to the end of the therapy or the transition to maintenance ECT. The final time point (t3) was 3 to 4 months after the end of the treatment for a follow-up evaluation.

We followed standard ECT stimulation protocols including initial titration starting with 800 mA, 0.75 ms pulse width at 20 Hz and duration of 1 s, representing a total delivered charge of 24 mC and then incrementing parameters until triggering a generalised seizure. After determining the seizure threshold, ECT parameters were defined as 6 times the trigger charge for right unilateral electrode placement and 3 times – for bilateral temporal electrode placement. Patients received two ECT sessions per week, with right unilateral electrode placement ($n = 3$) or bilateral temporal electrode placement ($n = 6$), for a total number of 8 to 12 sessions depending on the clinical response. For anaesthesia, we used etomidate and succinylcholine.

2.2. MRI data acquisition and map calculation

We acquired neuroimaging data on a 3T whole-body MRI system using 20-channel radiofrequency (RF) head and body coil for transmission (Magnetom Prisma, Siemens Medical Systems, Germany). The qMRI protocol consisted of three spoiled multi-echo 3D fast low-angle shot (FLASH) acquisitions with T1-, proton density- and magnetisation transfer weighting at 1 mm isotropic resolution (Weiskopf et al., 2013) and

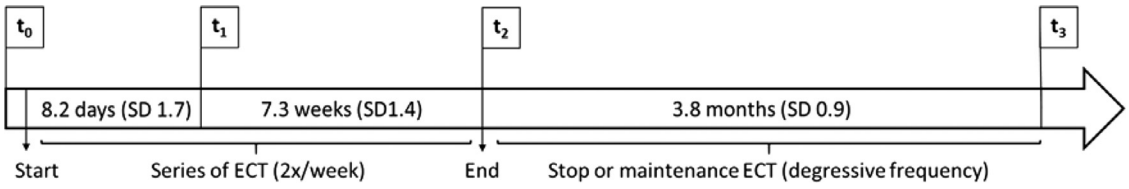

Fig. 1. Timeline of the study.

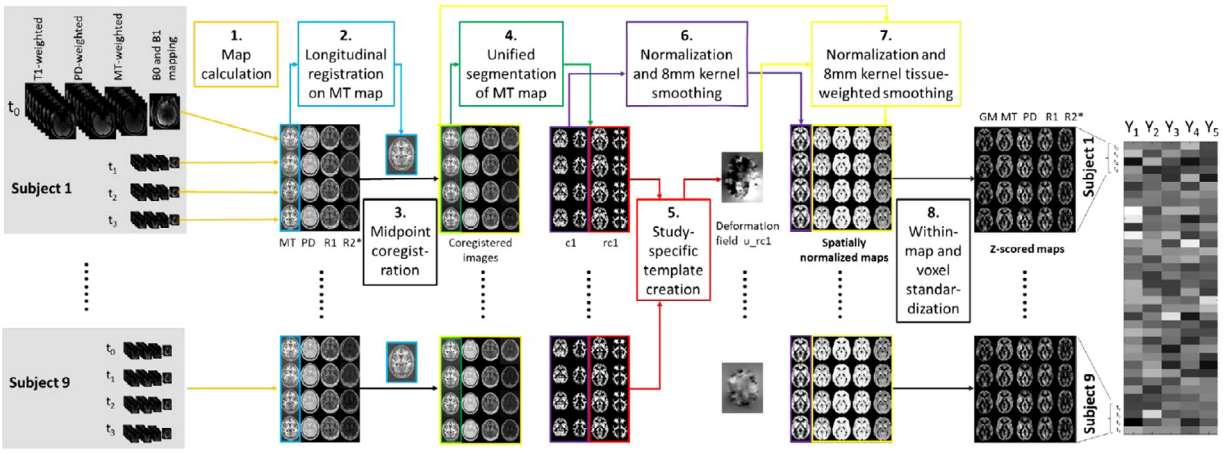

Fig. 2. Overview of the pre-processing pipeline. PD = proton density, MT = magnetization transfer, R1 = relaxation rate R1, R2* = relaxation rate R2*, c1 = grey matter probability map in native space, rc1 = DARTEL imported grey matter probability map, u_rc1 = deformation field.

additional B1 acquisition to map spatial inhomogeneities of the RF transmit field (Lutti et al., 2010, Lutti et al., 2012). We calculated quantitative maps of proton density (PD), longitudinal relaxation rate (R1), transversal relaxation rate R2* and magnetisation transfer (MT) saturation using in-house routines in the framework of SPM12 (Wellcome Centre for Human Neuroimaging, London, UK; https://www.fil.ion.ucl.ac.uk/spm/) running under Matlab 2017a (Mathworks, Sherborn, MA, USA). The set of echoes for each weighting were averaged to increase the signal-to-noise ratio (Helms et al., 2008) to calculate then the multi-parameter maps (MPMs) of MT saturation and R1, whilst R2* was derived from the TE dependence of the signal from all multi-echo acquisitions (Weiskopf et al., 2013). PD maps were derived from the averaged multi-echo FLASH data after scaling with the white matter signal (22) and after adjustment for receive sensitivity differences.

2.3. Longitudinal data pre-processing

Fig. 2 provides a detailed overview of the multi-step longitudinal registration of MRI data. We used SPM12s longitudinal diffeomorphic toolbox Ashburner and Ridgway (2013) that we adapted to the MPM. The "serial" longitudinal registration step created within-subject midpoint average from the MT saturation maps. Midpoint averages were used for tissue classification in grey and white matter maps following SPM12s "unified segmentation" approach with enhanced tissue priors (Lorio et al., 2016). Aiming to avoid contamination of tissue property estimates with the expected volume changes over time we performed within-subject affine registration of the multi-parameter and grey matter maps across time points to the midpoint average, instead of applying the spatial deformation between each time-point and the midpoint average as recommended previously (Ziegler et al., 2019). This was followed by diffeomorphic registration to MNI space using DARTEL Ashburner (2007) that provided optimal spatial registration parameters by creating a study-specific template. For the voxel-based morphometry (VBM) analysis the spatial registration procedure included scaling the grey matter tissue probability maps by the JacD of the deformation field (i.e. "modulation") obtained in the diffeomorphic step followed by spatial smoothing with an isotropic Gaussian smoothing kernel of 6 mm full-width-at-half-maximum (FWHM). For the voxel-based quantification (VBQ) analysis we used the previously described "weighted-averaging" procedure, which registers tissue-specific MPMs to MNI space while preserving the total of parameter values within each tissue class (Draganski et al., 2011).

Given that the scale of MPM data can vary with a factor of more than 100 we standardised all maps – grey matter (GM) volume, PD, MT, R1, R2* across subjects and time points by calculating at the voxel level the grand mean and standard deviation to then subtract the grand mean and divide by the standard deviation. This step of within-contrast and within-voxel standardisation was implemented to ensure the estimation and comparison of each dependent variable's contribution in the multivariate analysis. All statistical analyses were performed on the standardised data set.

2.4. Statistical analysis

The change of depression score over time was tested using a linear mixed-model with the fixed effect factor time (4 levels: t0, t1, t2, t3) and a random intercept for each subject. For model estimation, we used the *nlme* package in R 3.6.0 followed by post hoc tests in the *emmeans* package (Pinheiro et al., 2013, Lenth, 2019). Posthoc t-tests were corrected for multiple comparisons using Tukey's method Tukey (1949).

2.5. Multivariate general linear model implementation

We implemented the multivariate General Linear Model in Matlab as an SPM12 toolbox (see code availability).

Matrix of observations Y, at each voxel, Y consisted in 180 observations (9 individuals × 4 time points × 5 maps) organised in 5 columns $\{Y_1, Y_2, Y_3, Y_4, Y_5\}$ where Y_1 is the vector of grey matter volume values, Y_2 – of PD*, Y_3 – of MT saturation, Y_4 – of R1 and Y_5 – of R2*. Each column of Y included 36 observations (9 individuals × 4 time points) ordered by subject (S) and time point (t): $Y_j = \{S_1t_0, S_1t_1, S_1t_2, S_1t_3, S_2t_0, S_2t_1, \ldots, S_9t_3\}$.

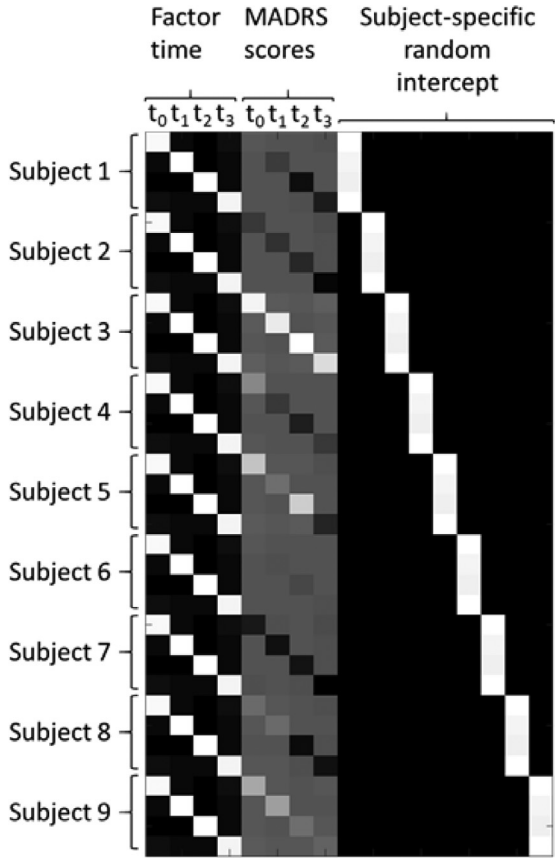

Fig. 3. Design matrix X. Allows for testing brain anatomy changes over time and for their interactions with symptoms improvement, whilst considering repeated measurements. The first four columns represent the four time points $t = \{t_0, t_1, t_2, t_3\}$, the next five columns – interaction term of MADRS score and time. The last nine columns represent random intercept for each subject coded as dummy variables.

Design matrix X: The design matrix included the four time points (t0, t1, t2, t3) as indicator variables. We also included the individuals' interaction terms of MADRS score x time as covariates and finally, to adjust for repeated measurements - we added a random intercept for each subject coded as a dummy variable (Fig. 3).

Multivariate GLM equations: The multivariate general linear model equation models the multivariate observations (see Fox (2015)) as follow:

$$Y = X\mathrm{B} + E \tag{1}$$

Critically, Y and X are multivariate matrices with $Y = \{Y_1, Y_2, \ldots, Y_m\}$ resulting from the concatenation of m dependent variables vectors of length N and X represents $N \times p$ matrix of predictors. Thus B is also a matrix of size $p \times m$ matrix of regression coefficients. E of size $N \times m$ containes residuals (see Fig. 4 for the particular implementation and matrix size of the multivariate GLM estimated in this study). It is of note that in the special case of $m = 1$, the equation corresponds to the univariate GLM equation.

Assumption of multivariate GLM: The assumptions pertain to the error term and assume that each i^{th} row of the error term, denoted ε_i' has a multivariate distribution of the form:

$$\varepsilon_i' \sim N_m(0, \Sigma) \tag{2}$$

With Σ a nonsingular error-covariance matrix, constant across observations. In addition, ε_i' and $\varepsilon_{i'}'$ are independent when $i \neq i'$.

Model estimation: We estimated the matrix B of coefficients using ordinary least-square estimation:

$$B = \left(X'X\right)^{-1}X'Y \tag{3}$$

Variance partitioning: The matrix of predicted value $\hat{Y}$ is equal to:

$$\hat{Y} = X\hat{B} \tag{4}$$

And the matrix of residual E is equal to:

$$E = Y - \hat{Y} = Y - X\hat{B} \tag{5}$$

The total sum-of-square-and-cross-product ($SSCP$) matrix of the model is:

$$SSCP_{Total} = Y'Y - N\bar{y}\bar{y}' \tag{6}$$

And can be partitioned into regression $SSCP_{Reg}$ and residual $SSCP_{Error}$:

$$SSCP_{Total} = SSCP_{Reg} + SSCP_{Error} = \left(\hat{Y}'\hat{Y} - N\bar{y}\bar{y}'\right) + E'E \tag{7}$$

Test statistics for global significance: To estimate the global significance of the GLM, i.e. testing the null hypothesis that all the coefficients in B are equal to zero, we can compute the product of $SSCP_{Reg}$ by the inverse of $SSCP_{Error}$:

$$SSCP_{Reg}SSCP_{Error}^{-1} = \frac{\hat{Y}'\hat{Y} - N\bar{y}\bar{y}'}{E'E} \tag{8}$$

And compute the eigenvalues of the resulting matrix following the general equation of eigen-decomposition with A a matrix for which we want to calculate the eigenvalues λ and eigenvectors:

$$\begin{aligned} Av &= \lambda v \\ Av - \lambda v &= 0 \\ (Av - \lambda I)v &= 0 \\ \det(A - \lambda I) &= 0 \end{aligned} \tag{9}$$

Then, by introducing the product of $SSCP_{Reg}$ by the inverse of $SSCP_{Error}$ into A and solving Eq. 9 we can find m eigenvalues λ:

$$det\left(\frac{\hat{Y}'\hat{Y} - N\bar{y}\bar{y}'}{E'E} - \lambda I_m\right) = 0 \tag{10}$$

The Wilk's lambda summary statistics Λ can then be calculated as a function of the m largest eigenvalues λ (Tabachnick et al., 2007):

$$\Lambda = \prod_{j=1}^{m} \frac{1}{1 + \lambda_j} \tag{11}$$

Then, statistical significance of Λ can be evaluated using an approximation to F:

$$F(df_1, df_2) = \left(\frac{1 - \Lambda^{1/s}}{\Lambda^{1/s}}\right)\left(\frac{df_2}{df_1}\right) \tag{12}$$

With

$$\begin{aligned} df_1 &= lq \\ df_2 &= rt - 2u \end{aligned} \tag{13}$$

And with

$$l = rank(Y) \tag{14}$$

$$q = rank(X) \tag{15}$$

$$u = \frac{df_1 - 2}{4} \tag{16}$$

$$r = N - q - \frac{lq + 1}{2} \tag{17}$$

$$t = \begin{cases} \frac{l^2q^2 - 4}{l^2 + q^2 - 5} \; if \; l^2 + q^2 - 5 > 0 \\ 1 \; if \; l^2 + q^2 - 5 \leq 0 \end{cases} \tag{18}$$

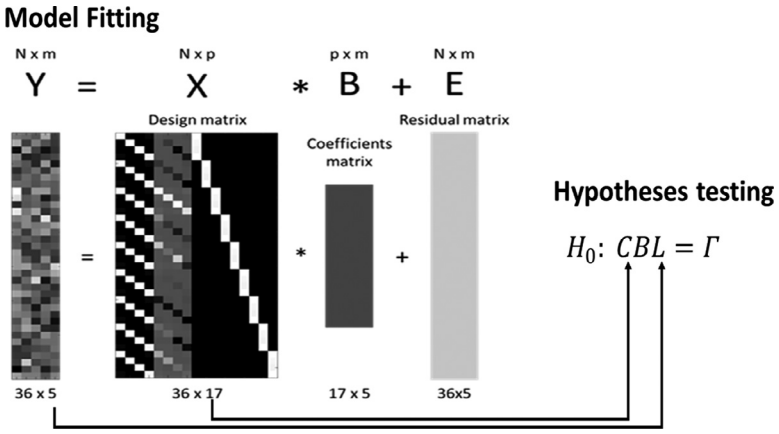

Fig. 4. Multivariate GLM hypotheses testing. A multivariate model is fitted at each voxel to the multi-time points and multi-contrasts data, with a design matrix X encoding for the effect of time and clinical measures. Hypotheses testing use the regression B and the residual E to test specific questions encoded in the contrasts matrices C and L.

$if\ \min(l, q) \leq 2$, then the F-approximation is exact.

Test statistic for specific contrasts: Testing specific hypothesis about the relationship between all or a subset of the dependent variables and contrasts between predictors involves the following linear hypothesis (Fox et al., 2013):

$$H_0 : CBL = \Gamma \tag{19}$$

With L a $m \times h$ hypothesis matrix on the column of B, with $h \leq m$, i.e. a combination of h dependent variables, C a $v \times p$ response transformation matrix on the rows of B, with $v \leq p$, i.e. a combination of v predictors, and the right-hand-side Γ, a matrix of constant set in our case as the null matrix. The $SSCP_{Hyp}$ and $SSCP_{Error}$ can be therefore calculated as:

$$\begin{aligned} SSCP_{Hyp} &= \left(C\hat{B}L'\right)'\left[C\left(X'X\right)^{-1}C'\right]\left(C\hat{B}L'\right) \\ SSCP_{Error} &= L\left(\hat{E}'\hat{E}\right)L' \end{aligned} \tag{20}$$

And a test statistic under the null hypothesis follows the same logic as in Eq. 8–11 with few modifications. First, the Wilk's Λ (Eq. 11) becomes a function of the h largest eigenvalues (previously m) and Eq. 14, 15, 17 are replaced by Eq. 21, 22 and 23, respectively:

$$l = rank(L) \tag{21}$$

$$q = rank(C) \tag{22}$$

$$r = N - rank(X) - \frac{lq+1}{2} \tag{23}$$

Canonical vector computation: When the hypothesis matrix L involves multiple dependent variables ($q > 1$), it is of interest to extract the contribution of each dependent variable, also called canonical vector, to the test statistic Λ. This contribution corresponds to the eigenvectors of the eigendecomposition of the product of $SSCP_{Reg}$ by the inverse of $SSCP_{Error}$ (Eq. 8). This can be done by simply solving Eq. 9 for each eigenvalue $\lambda = (\lambda_1, \cdots, \lambda_h)$ (Tabachnick et al., 2007). For example, the first eigenvector, or first canonical vector can be calculated by solving Eq. 8 for λ_1. It is worth noting that in order to be able to compare the values of the canonical vector, the columns of Y must be put on the same scale.

*Hypotheses matrices L:*To test for the joint effect on the 5 MRI maps we set the following linear $m \times h$ L contrast matrix (with m the total number of dependent variables and h the number of dependent variables involved in the contrast). In the case of the joint analysis on all maps, the contrast matrix is the 5×5 identity matrix:

$$L_{all\ maps} = \begin{bmatrix} 1 & 0 & 0 & 0 & 0 \\ 0 & 1 & 0 & 0 & 0 \\ 0 & 0 & 1 & 0 & 0 \\ 0 & 0 & 0 & 1 & 0 \\ 0 & 0 & 0 & 0 & 1 \end{bmatrix}$$

Of note, the following L contrasts would perform classical univariate analysis on each column of Y.

$$L_{GM} = \begin{bmatrix} 1 \\ 0 \\ 0 \\ 0 \\ 0 \end{bmatrix} L_{PD} = \begin{bmatrix} 0 \\ 1 \\ 0 \\ 0 \\ 0 \end{bmatrix} L_{MT} = \begin{bmatrix} 0 \\ 0 \\ 1 \\ 0 \\ 0 \end{bmatrix} L_{R1} = \begin{bmatrix} 0 \\ 0 \\ 0 \\ 1 \\ 0 \end{bmatrix} L_{R2^*} = \begin{bmatrix} 0 \\ 0 \\ 0 \\ 0 \\ 1 \end{bmatrix}$$

Change of MRI parameters over time: The following $v \times p$ C matrices of contrasts (with v the number of predictors involved in the contrast and p the total number of predictors, $p = 17$ in this case) were intended to test for: the early effect of ECT (the effect that occurs between the time interval t_0 to t_1)

$$C = \begin{bmatrix} 1 & 0 & 0 & \cdots & 0 \\ 0 & 1 & 0 & \cdots & 0 \end{bmatrix}$$

the effect of a complete series of ECT (the effect that occurs between the time interval t_0 to t_2)

$$C = \begin{bmatrix} 1 & 0 & 0 & 0 & \cdots & 0 \\ 0 & 0 & 1 & 0 & \cdots & 0 \end{bmatrix}$$

the long-term effect of ECT (the effect that occurs between the time interval t_0 to t_3)

$$C = \begin{bmatrix} 1 & 0 & 0 & 0 & 0 & \cdots & 0 \\ 0 & 0 & 0 & 1 & 0 & \cdots & 0 \end{bmatrix}$$

the late effect of ECT (the effect that occurs between the time interval t_2 to t_3)

$$C = \begin{bmatrix} 0 & 0 & 1 & 0 & 0 & \cdots & 0 \\ 0 & 0 & 0 & 1 & 0 & \cdots & 0 \end{bmatrix}$$

Association between MRI parameters and symptom severity changes over time: Additionally, we also set C contrasts matrices intended to test for the association between the change of MRI maps and change of MADRS score. We first set a C contrast matrix intended to test for any association between the change of MRI maps and symptoms between baseline and one week of treatment (t_0 to t_1), between baseline and after the ECT series (t_0 to t_2) and between baseline and at 6 months follow-up (t_0 to t_3):

$$C = \begin{bmatrix} 0 & 0 & 0 & 0 & -1 & 1 & 0 & 0 & 0 & \cdots & 0 \\ 0 & 0 & 0 & 0 & -1 & 0 & 1 & 0 & 0 & \cdots & 0 \\ 0 & 0 & 0 & 0 & -1 & 0 & 0 & 1 & 0 & \cdots & 0 \end{bmatrix}$$

Then to identify the specific time interval were an association between a change of MRI map and change of symptom is present, we tested the following three C contrast matrices:

$$C = \begin{bmatrix} 0 & 0 & 0 & 0 & -1 & 1 & 0 & 0 & 0 & \cdots & 0 \end{bmatrix}$$

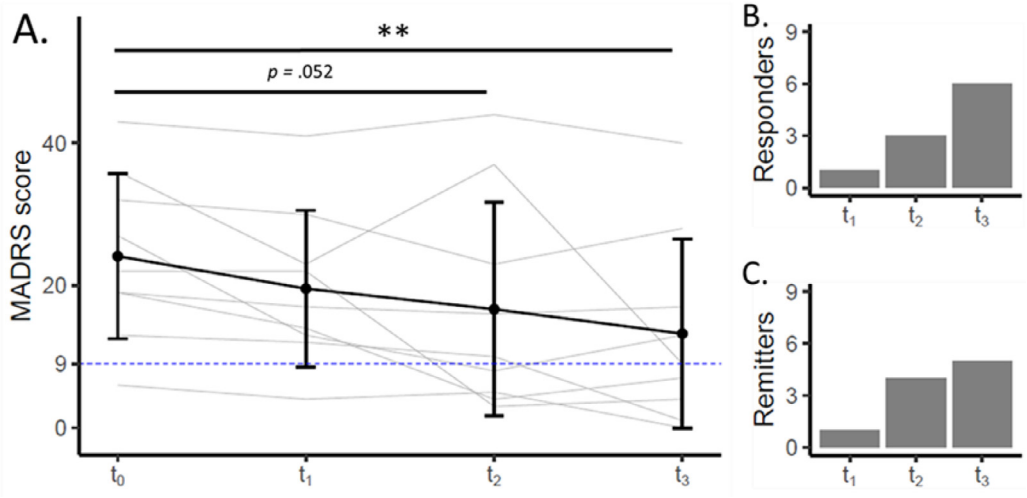

Fig. 5. A. Evolution of depressive symptoms as measured by the MADRS. Black dots and error bars represent mean and standard deviation respectively. Grey lines represent individual trajectories. The blue dashed line corresponds to the remission threshold (defined as a MADRS score below or equal to 9). ** = p < .01 corrected for multiple comparisons using Tukey's method. **B.** Count of responder and non-responder patients at t1, t2 and t3. C. Count of remitters and non-remitters' patients at t1, t2 and t3.

$$C = \begin{bmatrix} 0 & 0 & 0 & 0 & -1 & 0 & 1 & 0 & 0 & \cdots & 0 \end{bmatrix}$$

$$C = \begin{bmatrix} 0 & 0 & 0 & 0 & -1 & 0 & 0 & 1 & 0 & \cdots & 0 \end{bmatrix}$$

Results were reported significant with a statistical threshold $P < .05$ at the cluster-level after family-wise error (FWE) correction for multiple comparisons using Gaussian Random Field Theory over the whole brain's grey matter.

3. Results

3.1. Symptom severity

ECT treatment reduced depression severity assessed with the MADRS score (main effect of time $F(3, 24) = 6.84, p < .01$). Post-hoc tests of ECTs effects on symptom severity over separate time intervals showed borderline significant MADRS reduction at t2 compared with t0 (mean difference = 7.44, standard error (SE) = 2.72, $t = 2.7$, $p = .052$) and strong MADRS decrease at t3 compared with t0 (mean difference = 10.89, SE = 2.7, $t = 4$, $p < .01$) (see Fig. 5 A.). At t2, 33% patients showed response to ECT and 44% were in remission. At t3, 66% of the patients were responders and 56% in remission (see Fig. 5 B and C).

3.2. Brain volume and tissue properties

Effect of acute ECT series. Between t0 to t2, we observed ECT induced brain anatomy changes in an area encompassing the right hippocampus and right para-hippocampal gyrus additionally to the right anterior cingulate gyrus (pFWE < .05 at the cluster level) (see Fig. 6 and Suppl. Table 1). The weights attributed to each dependent variable revealed a predominant contribution of GM volume to the effects.

Long-term ECT effects. The differential contrast between t0 to t3 showed brain anatomy changes in the entorhinal cortex, inferior temporal gyrus and temporal pole on the left (pFWE < .05 at the cluster and peak levels). GM volume changes were the main contributors to the observed effects (see Fig. 7 and Suppl. Table 2).

There were no significant effects for the contrast testing for differences between t2 and t3.

Association with symptom severity. The statistical contrast testing for association between brain anatomy and symptom severity changes for the time intervals t0 and t1, t0 and t2 and t0 and t3 demonstrated a widespread anatomical pattern comprising precuneus, hippocampal complex/amygdala, ventromedial prefrontal cortex/anterior cingulate and the ventral striatum on the left (Fig. 8 and Suppl. Table 3). GM volume changes mainly drove the ECT effects on precuneus and the mesial temporal lobe associated with symptom severity. Whilst, myelin and tissue free water drove the effect in the ventromedial prefrontal cortex and the anterior cingulate. The ventral striatum changes were due to iron content.

When investigating the association between ECT-induced brain anatomy and symptom severity changes within each time interval separately, we demonstrate that the effects observed in the exploratory contrast were entirely driven by the treatment period (between t0 and t3, all clusters significant at cluster level FWE). Here, we show an almost identical pattern, however, with bilateral effects on hippocampal complex/amygdala and ventral striatum (Fig. 9 and Suppl. table 4).

4. Discussion

In this longitudinal study, we investigate the temporal trajectory of ECT-induced brain anatomy changes enriching morphometry assessment with quantitative MRI estimates indicative for myelin, tissue water and iron content. Aiming to tell apart the contribution of brain volume and tissue properties, we adapt the established SPM12 longitudinal spatial registration algorithm to longitudinal multi-parameter data and introduce a dedicated multivariate GLM analysis framework. We show that ECT-induced hippocampus volume changes are not associated with focal increase in brain tissue water as seen in oedema. The observed spatial pattern of volume and tissue property changes confined to the anterior cingulate, hippocampus, ventral striatum and precuneus correlated with the individuals' long-term clinical outcome. We interpret our findings in the context of current models of ECT-induced beneficial effects on depression.

Our main finding is that the observed ECT-related hippocampus volume increase was not paralleled by changes in estimates of brain's tissue water content. This empirical evidence contradicts speculations about seizure-induced vasogenic or cytotoxic oedema of the mesial temporal lobe that could be misinterpreted as ECT effect on hippocampus volume in computational anatomy studies. Besides one single study reporting ECT-associated mean diffusivity increase that can be interpreted as tissue oedema (Repple et al., 2019), most recent reports showed mean diffusivity reduction in the hippocampus and adjacent white mat-

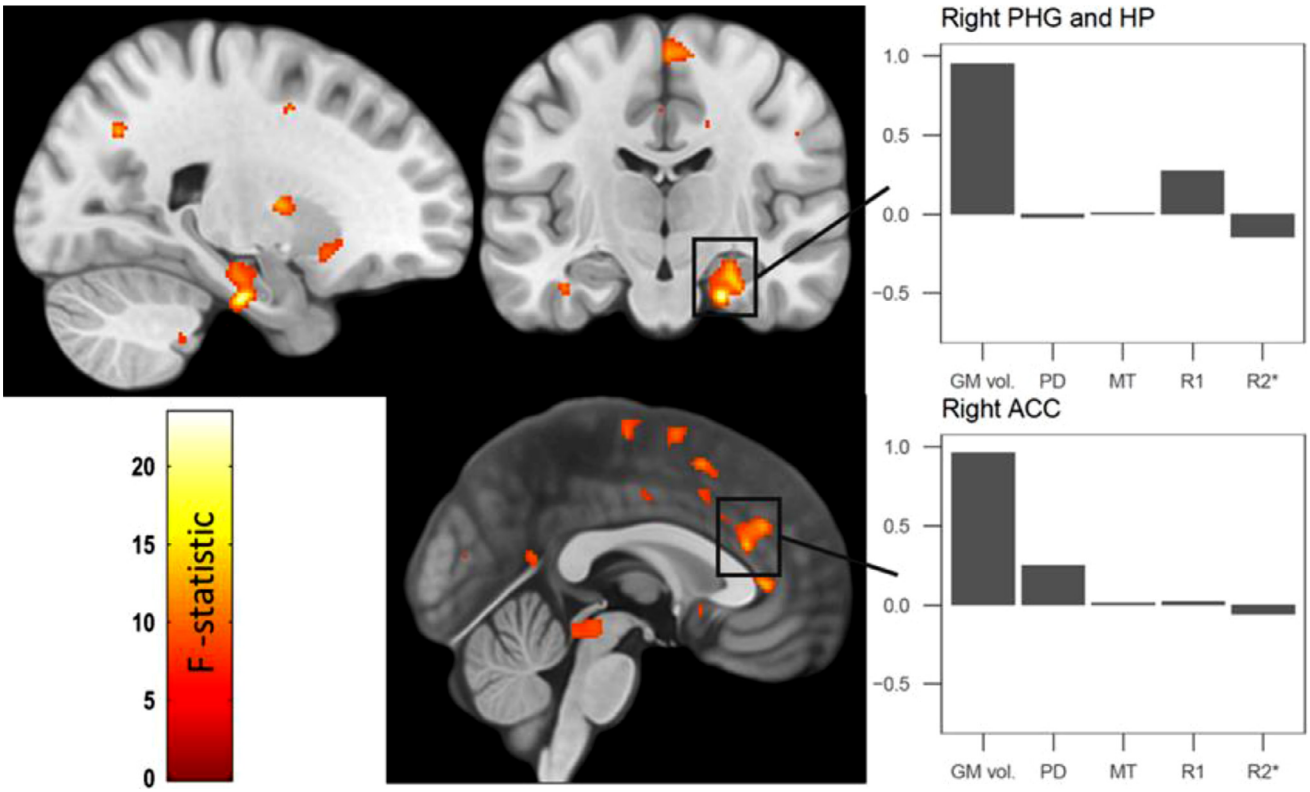

Fig. 6. Statistical parametric map of the multivariate analysis of differences between t0 and t2. For presentation purposes displayed at p < .001 uncorrected. Grey bars represent the canonical vector of the data matrix Y (arbitrary unit). PHG = para-hippocampal gyrus, HP = hippocampus, ACC = anterior cingulate gyrus.

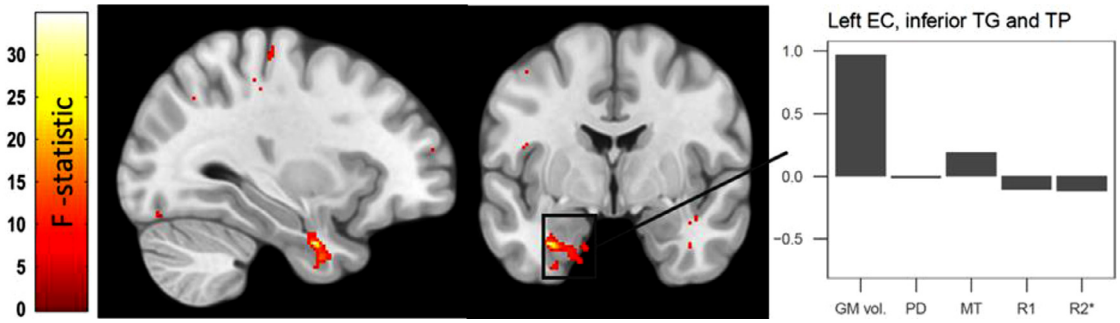

Fig. 7. Statistical parametric map of the multivariate analysis of differences between t0 and t3. For presentation purposes displayed at p < .001 uncorrected. Grey bars represent the canonical vector of the data matrix Y (arbitrary unit). *EC = entorhinal cortex, TG = temporal gyrus, TP = temporal pole.*

ter (Nuninga et al., 2020, Jorgensen et al., 2016, Kubicki et al., 2019, Lyden et al., 2014). Given the specificity of the PD maps to tissue water content Tofts (2004), we see the absence of PD changes contrasted against ECT-induced hippocampus volume increase as unique evidence against the assumption of seizure-associated oedema. Given the biophysical model behind the relaxometry-based brain tissue quantification, we interpret our PD* findings as lack of ECT-induced increase of MRI visible unbound tissue water in the brain parenchyma rather than intracellular oedema due to increased ion influx into neurons (Camilleri et al., 2020). This is a novel finding that overcomes the limitation of the recently published multi-contrast MRI study (Nuninga et al., 2020) by combining all parameter maps within one design matrix rather than testing each parameter in separate linear models. The plausibility of the current findings is confirmed by the predicted and observed changes in the right anterior hippocampus and in the right ACC, regions reported in recent ECT studies and meta-analyses (James et al., 2018, Dukart et al., 2014, Cano et al., 2019, Gbyl and Videbech, 2018, Ota et al., 2015, Pirnia et al., 2016, Cano et al., 2017).

Challenged by mainly negative findings on the association between ECT-induced brain plasticity changes and clinical outcome (Oltedal et al., 2018), we tested in a whole-brain analysis the association between volume, tissue properties and change of depression scores over time. Our analysis demonstrated a widespread pattern of association between ECT-related depression severity improvement and anatomy changes in left precuneus, hippocampus, anterior cingulate and left ventral striatum. The distributed spatial pattern of associations between ECT-induced symptom improvement and brain anatomy changes largely overlaps with most recent cross-sectional results from a mega-analysis including ca 200 ECT treated patients (Mulders et al., 2020). Besides lending credibility to our findings on association between brain tissue properties and clinical outcome, these results indicate that alongside limbic regions, the ventrolateral and medial PFC are involved in the anti-depressant effects of ECT. Particularly intriguing is the consistency of ECT-related anatomy, perfusion and metabolism findings in the precuneus (Leaver et al., 2015, Leaver et al., 2019, Chau et al., 2017), which, given its central role in self-centred mental imagery strategies

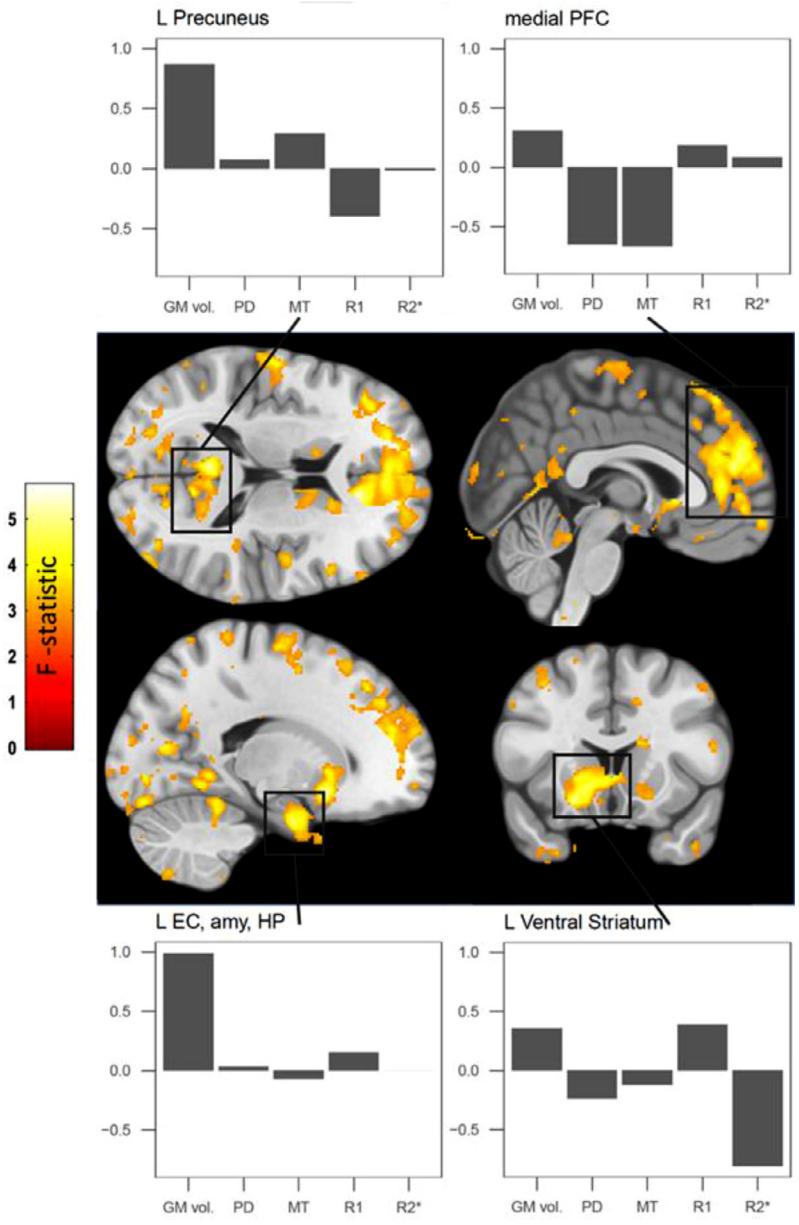

Fig. 8. Statistical parametric map of the the multivariate association with change of depression severity between t0 and t1, t0 and t2 and t0 and t3. For presentation purposes displayed at $p < .001$ uncorrected. Grey bars represent the canonical vector of the data matrix Y (arbitrary unit). *PFC = prefrontal cortex, EC = entorhinal cortex, amy = amygdala.*

and successful episodic memory retrieval, could explain a large amount of depression associated symptoms (Cavanna and Trimble, 2006).

Previous research reported associations between clinical outcome after ECT and anatomical regions partially overlapping with the presented pattern, however the interpretation was limited to descriptive morphometry changes or water diffusion properties (Kubicki et al., 2019, Yrondi et al., 2019). The observed correlation between ECT-associated clinical improvement and anatomy changes went beyond the expected effects on the anterior "limbic" hippocampus volume to show associations with precuneus volume. Although not supported by the findings of recent mega-analyses (Oltedal et al., 2018 , Ousdal et al., 2020), we explain the discrepancy by the fact that our volume measurements are derived from qMRI data reducing the probability of "spurious" morphometric findings based on T1-weighted protocols (Natu et al., 2019, Lorio et al., 2016). ECT-induced reduction in depression severity was associated with changes in myelin and tissue water content in the anterior cingulate. We interpret this finding in light of intracortical myelin plasticity within limbic networks assessed by the MT saturation, which is further paralleled by alterations in MR-visible water content captured by PD*. Ventral striatum correlations with symptom reduction were explained by iron and volume changes that, given the essential role of iron in dopamine synthesis (Rouault, 2013), can be potentially linked to ECT-induced changes in the spatial gradient of dopamine receptor distribution in this "limbic" part of the basal ganglia. Interpretations based on the temporal trajectory of our findings make it difficult to distinguish what comes first - normalisation of activity in limbic networks or restoration of the regulatory ability of medial prefrontal regions. Studying the course of brain plasticity changes during the ECT treatment with a finer temporal resolution could help to better understand the sequence of events leading to therapeutic benefits, and thus, define what brain regions should be primarily targeted to alleviate depressive symptoms.

Another novel aspect of our study is the adaptation of longitudinal spatial registration algorithms to parameter maps and the implementation of a dedicated multivariate analytical framework. Although consistent with the previously suggested spatial registration for parameter maps, we minimise the potential impact of morphometry changes on the quantitative tissue property metrics by applying only affine transformations to individual's different time point acquisitions rather than

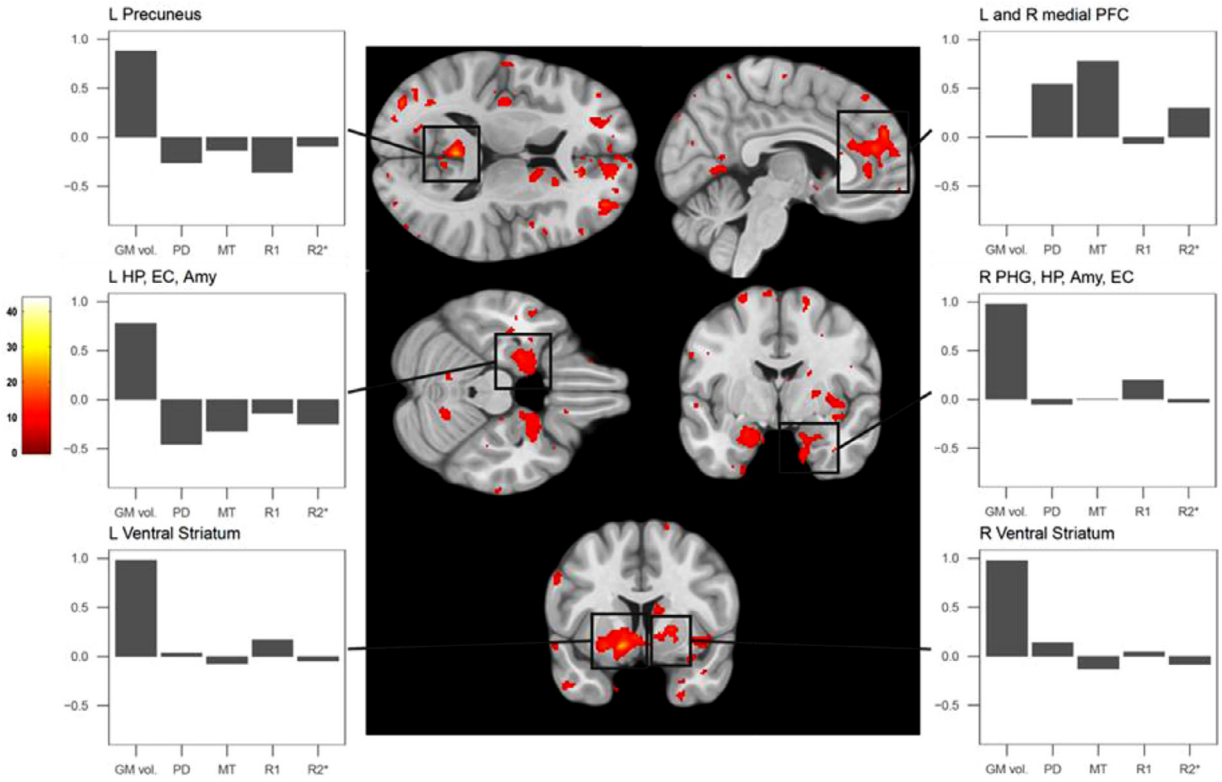

Fig. 9. Statistical parametric map of the multivariate association with change of depression severity between t0 and t3. For presentation purposes displayed at $p < .001$ uncorrected. Grey bars represent the canonical vector of the data matrix Y (arbitrary unit). *PFC = prefrontal cortex, EC = entorhinal cortex, amy = amygdala, HP = hippocampus, PHG = para-hippocampal gyrus.*

non-linear transformation estimates based on morphometry data. This, in our opinion, together with the inclusion of volume maps in the multivariate GLM, reduces the potential contamination effect of parameters indicative of tissue properties by the estimates of volume change over time. Along these lines, the proposed multivariate approach, when compared to classical multiple univariate models, reduces the probability of type I errors due to the fact that we estimate one model where all maps are jointly tested within a single contrast.

Here, we address potential limitations of our strategy concerning multiple comparisons correction. Mass univariate whole-brain neuroimaging analyses involve model estimation at each voxel, typically resulting in the estimation of multiple separate GLMs that require correction for multiple comparisons using the random field theory (Brett et al., 2003) after estimation of data smoothness (Kiebel et al., 1999). Given that this estimation is performed on the standardised residuals of the fitted GLMs, it becomes non-trivial in the multivariate GLM as the residuals are multivariate. We are currently investigating this aspect in greater detail. Another limitation is pertinent to the interpretation of results in the context of the multivariate GLM. Here, we only reported the canonical vector at the peak voxel of the clusters, which may not be representative of the overall pattern in the cluster. We are currently unable to summarise and assess the homogeneity or heterogeneity of the profile of the canonical vectors belonging to a given cluster. Additionally, the interpretation of the results is limited by the absence of directionality of effects based on F-tests.

Despite the anatomically plausible patterns of ECT-induced anatomy changes and the consistency with previous research on the topic (Ousdal et al., 2020, Bouckaert et al., 2016), we consider potential drawbacks of underpowered studies. Given the sample size of nine individuals, we acknowledge the potential effects of an underpowered study on effect size estimation and the fact that we face a high sampling variability. The longitudinal character of the study may reduce to a certain extent the inherent sampling variability and in particular, the heterogeneity in terms of underlying clinical diagnosis - major depressive disorder, bipolar disorder and schizoaffective disorder, considering the notion of associated differential brain anatomy patterns (Rubin-Falcone et al., 2018, Chang et al., 2018, MacMaster et al., 2014, Niu et al., 2017). Under the assumption that each individual is his/her own control and there is no interaction between specific affective disorder and ECT treatment, we ascribe the observed anatomy changes to the effects of ECT (Dukart et al., 2014).

In summary, we present unique findings on the temporal trajectory of ECT-induced brain volume and tissue property changes using quantitative MRI and multivariate statistics. Our observation of hippocampus volume change in the absence of concomitant changes in tissue water content provide strong empirical evidence against the assumption that the consistently reported ECT-associated morphometry differences are related to tissue oedema as seen in status epilepticus. The proposed longitudinal data processing and multivariate analysis framework can be readily used with multi-contrast and longitudinal MRI data to further foster neuroimaging informed clinical guidelines and decision making in psychiatry.

Credit autor statement

Conception and design of the study: LG, FK and BD.

Acquisition and analysis of data: LG, CR, JFM, KSL, DS, AL, AvG, FK, BD.

Drafting a significant portion of the manuscript or figures: LG, CR, JFM, KSL, DS, AL, AvG, FK, BD.

Code availability

The code used to run the multivariate analysis on the neuroimaging data is available as SPM toolbox at https://github.com/LREN-CHUV/MSPM

Data availability

Anonymised metadata can be made available after a reasonable request to the Authors following a formal data sharing agreement.

Acknowledgments and Funding

We would like to thank all participants in the study. BD is supported by the Swiss National Science Foundation (NCCR Synapsy, project grants Nr. 32003B_135679, 32003B_159780, 324730_192755 and CRSK-3_190185) and the Leenaards Foundation. The research leading to these results has received funding from the European Union's Horizon 2020 research and innovation program under grant agreement No. 720270 (HBP SGA1). This work was carried out on the MRI platform of the Département des Neurosciences Cliniques - Centre Hospitalier Universitaire Vaudois (CHUV), which is generously supported by the ROGER DE SPOELBERCH and Partridge Foundations. AL is supported by the ROGER DE SPOELBERCH foundation and the Swiss National Science Foundation (320030_184784).

Supplementary materials

Supplementary material associated with this article can be found, in the online version, at doi:10.1016/j.neuroimage.2021.117895.

References

James, SL, Abate, D, Abate, KH, Abay, SM, Abbafati, C, Abbasi, N, et al., 2018. Global, regional, and national incidence, prevalence, and years lived with disability for 354 diseases and injuries for 195 countries and territories, 1990–2017: a systematic analysis for the global burden of disease study 2017. The Lancet 392 (10159), 1789–1858.

The UK ECT REVIEW GROUP, 2003. Efficacy and safety of electroconvulsive therapy in depressive disorders: a systematic review and meta-analysis. The Lancet 361 (9360), 799–808.

Read, J, Cunliffe, S, Jauhar, S, McLoughlin, DM., 2019. Should we stop using electroconvulsive therapy? BMJ k5233.

Ueno, M, Sugimoto, M, Ohtsubo, K, Sakai, N, Endo, A, Shikano, K, et al., 2019. The effect of electroconvulsive seizure on survival, neuronal differentiation, and expression of the maturation marker in the adult mouse hippocampus. J. Neurochem. 149 (4), 488–498.

Argyelan, M, Oltedal, L, Deng, Z-D, Wade, B, Bikson, M, Joanlanne, A, et al., 2019. Electric field causes volumetric changes in the human brain. eLife 23, 8.

Dukart, J, Regen, F, Kherif, F, Colla, M, Bajbouj, M, Heuser, I, et al., 2014. Electroconvulsive therapy-induced brain plasticity determines therapeutic outcome in mood disorders. Proc. Natl. Acad. Sci. 111 (3), 1156–1161.

Joshi, SH, Espinoza, RT, Pirnia, T, Shi, J, Wang, Y, Ayers, B, et al., 2016. Structural plasticity of the hippocampus and amygdala induced by electroconvulsive therapy in major depression. Biol Psychiatry 79 (4), 282–292.

Leaver, AM, Vasavada, M, Joshi, SH, Wade, B, Woods, RP, Espinoza, R, et al., 2018. Mechanisms of antidepressant response to electroconvulsive therapy studied with perfusion magnetic resonance imaging. Biol. Psychiatry.

Nuninga, JO, Mandl, RCW, Boks, MP, Bakker, S, Somers, M, Heringa, SM, et al., 2020. Volume increase in the dentate gyrus after electroconvulsive therapy in depressed patients as measured with 7T. Mol. Psychiatry 25 (July(7)), 1559–1568.

Oltedal, L, Narr, KL, Abbott, C, Anand, A, Argyelan, M, Bartsch, H, et al., 2018. Volume of the human hippocampus and clinical response following electroconvulsive therapy. Biol. Psychiatry 84 (October 15(8)), 574–581.

Ousdal, OT, Argyelan, M, Narr, KL, Abbott, C, Wade, B, Vandenbulcke, M, et al., 2020. Brain changes induced by electroconvulsive therapy are broadly distributed. Biol. Psychiatry 87 (March 1(5)), 451–461.

Takamiya, A, Plitman, E, Chung, JK, Chakravarty, M, Graff-Guerrero, A, Mimura, M, et al., 2019. Acute and long-term effects of electroconvulsive therapy on human dentate gyrus. Neuropsychopharmacology 44 (September(10)), 1805–1811.

Wade, BSC, Sui, J, Hellemann, G, Leaver, AM, Espinoza, RT, Woods, RP, et al., 2017. Inter and intra-hemispheric structural imaging markers predict depression relapse after electroconvulsive therapy: a multisite study. Transl. Psychiatry 7 (12), 1–12.

Natu, VS, Gomez, J, Barnett, M, Jeska, B, Kirilina, E, Jaeger, C, et al., 2019. Apparent thinning of human visual cortex during childhood is associated with myelination. Proc. Natl. Acad. Sci. 116 (October 8(41)), 20750–20759.

Lorio, S, Kherif, F, Ruef, A, Melie-Garcia, L, Frackowiak, R, Ashburner, J, et al., 2016. Neurobiological origin of spurious brain morphological changes: a quantitative MRI study. Hum Brain Mapp. 37 (5), 1801–1815.

Kim, JA, Chung, J, Ho Yoon, Pyeong, Kim, Dong Ik, Chung, TS, Kim, EJ, et al., 2001. Transient MR signal changes in patients with generalized tonicoclonic seizure or status epilepticus: Periictal diffusion-weighted imaging. Am. J. Neuroradiol. 22 (6), 1149–1160.

Righini, A, Pierpaoli, C, Alger, JR, Di Chiro, G., 1994. Brain parenchyma apparent diffusion coefficient alterations associated with experimental complex partial status epilepticus. Magn. Reson. Imaging 12 (6), 865–871.

Szabo, K, Poepel, A, Pohlmann-Eden, B, Hirsch, J, Back, T, Sedlaczek, O, et al., 2005. Diffusion-weighted and perfusion MRI demonstrates parenchymal changes in complex partial status epilepticus. Brain 128 (6), 1369–1376.

Mander, AJ, Whitfield, A, Kean, DM, Smith, MA, Douglas, RH, Kendell, RE., 1987. Cerebral and brain stem changes after ECT revealed by nuclear magnetic resonance imaging. Br. J. Psychiatry J. Ment. Sci. 151, 69–71.

Scott, AIF, Douglas, RHB, Whitfield, A, Kendell, RE., 1990. Time course of cerebral magnetic resonance changes after electroconvulsive therapy. Br. J. Psychiatry 156 (APR.), 551–553.

Kunigiri, G, Jayakumar, PN, Janakiramaiah, N, Gangadhar, BN., 2007. MRI T2 relaxometry of brain regions and cognitive dysfunction following electroconvulsive therapy. Indian J. Psychiatry 49 (3), 195.

Tofts, PS., 2004. PD: proton density of tissue water. Quant. MRI Brain 83–109.

Szabo, K, Hirsch, JG, Krause, M, Ende, G, Henn, FA, Sartorius, A, et al., 2007. Diffusion weighted MRI in the early phase after electroconvulsive therapy. Neurol. Res. 29 (3), 256–259.

Nuninga, JO, Mandl, RCW, Froeling, M, Siero, JCW, Somers, M, Boks, MP, et al., 2020. Vasogenic edema versus neuroplasticity as neural correlates of hippocampal volume increase following electroconvulsive therapy. Brain Stimul. Basic Transl. Clin. Res. Neuromodulation 13 (4), 1080–1086.

Weiskopf, N, Mohammadi, S, Lutti, A, Callaghan, MF., 2015. Advances in MRI-based computational neuroanatomy: from morphometry to in-vivo histology. Curr. Opin. Neurol. 28 (4), 313–322.

Laule, C, Vavasour, IM, Kolind, SH, Li, DKB, Traboulsee, TL, Moore, GRW, et al., 2007. Magnetic resonance imaging of myelin. Neurotherapeutics 4 (3), 460–484.

Koenig, SH., 1991. Cholesterol of myelin is the determinant of gray-white contrast in MRI of brain. Magn. Reson. Med. 20 (2), 285–291.

Stüber, C, Morawski, M, Schäfer, A, Labadie, C, Wähnert, M, Leuze, C, et al., 2014. Myelin and iron concentration in the human brain: a quantitative study of MRI contrast. NeuroImage 93, 95–106.

Mezer, A, Yeatman, JD, Stikov, N, Kay, KN, Cho, N-J, Dougherty, RF, et al., 2013. Quantifying the local tissue volume and composition in individual brains with magnetic resonance imaging. Nat Med 19 (December(12)), 1667–1672.

Draganski, B, Ashburner, J, Hutton, C, Kherif, F, Frackowiak, RSJ, Helms, G, et al., 2011. Regional specificity of MRI contrast parameter changes in normal ageing revealed by voxel-based quantification (VBQ). NeuroImage 55, 1423–1434.

Weiskopf, N, Suckling, J, Williams, G, Correia, MM, Inkster, B, Tait, R, et al., 2013. Quantitative multi-parameter mapping of R1, PD*, MT, and R2* at 3T: a multi-center validation. Front. Neurosci. 7.

Gracien, R-M, Maiworm, M, Brüche, N, Shrestha, M, Nöth, U, Hattingen, E, et al., 2020. How stable is quantitative MRI? – assessment of intra- and inter-scanner-model reproducibility using identical acquisition sequences and data analysis programs. NeuroImage 207, 116364.

Stefani, A, Mitterling, T, Heidbreder, A, Steiger, R, Kremser, C, Frauscher, B, et al., 2019. Multimodal magnetic resonance imaging reveals alterations of sensorimotor circuits in restless legs syndrome. Sleep.

Fox, J., 2015. Applied Regression Analysis and Generalized Linear Models. Sage Publications.

McFarquhar, M, McKie, S, Emsley, R, Suckling, J, Elliott, R, Williams, S., 2016. Multivariate and repeated measures (MRM): a new toolbox for dependent and multimodal group-level neuroimaging data. NeuroImage 132, 373–389.

Stoyanov, D, Kandilarova, S, Paunova, R, Barranco Garcia, J, Latypova, A, Kherif, F, 2019. Cross-validation of functional MRI and paranoid-depressive scale: results from multivariate analysis. Front. Psychiatry. [Internet][cited 2020 Oct 28];10. Available from: https://www.frontiersin.org/articles/10.3389/fpsyt.2019.00869/full .

Zufferey, V, Donati, A, Popp, J, Meuli, R, Rossier, J, Frackowiak, R, et al., 2017. Neuroticism, depression, and anxiety traits exacerbate the state of cognitive impairment and hippocampal vulnerability to Alzheimer's disease. Alzheimers Dement. Diagn. Assess. Dis. Monit.. 7, 107–114.

Kherif, F, Poline, J-B, Flandin, G, Benali, H, Simon, O, Dehaene, S, et al., 2002. Multivariate Model Specification for fMRI Data. NeuroImage 16 (4), 1068–1083.

Ziegler, G, Hauser, TU, Moutoussis, M, Bullmore, ET, Goodyer, IM, Fonagy, P, et al., 2019. Compulsivity and impulsivity traits linked to attenuated developmental frontostriatal myelination trajectories. Nat. Neurosci. 22 (6), 992–999.

American Psychiatric Association, 2000. Diagnostic and Statistical Manual of Mental Disorders-IV Text Revision. APA, Wash DC.

Montgomery, SA, Åsberg, M., 1979. A new depression scale designed to be sensitive to change. Br. J. Psychiatry 134 (4), 382–389.

Zimmerman, M, Chelminski, I, Posternak, M., 2004. A review of studies of the Montgomery-Asberg depression rating scale in controls: implications for the definition of remission in treatment studies of depression. Int Clin Psychopharmacol 19 (1), 1–7.

Lutti, A, Hutton, C, Finsterbusch, J, Helms, G, Weiskopf, N., 2010. Optimization and validation of methods for mapping of the radiofrequency transmit field at 3T. Magn. Reson. Med. 64 (1), 229–238.

Lutti, A, Stadler, J, Josephs, O, Windischberger, C, Speck, O, Bernarding, J, et al., 2012. Robust and fast whole brain mapping of the RF transmit field B1 at 7T. PloS One 7 (3), e32379.

Helms, G, Dathe, H, Kallenberg, K, Dechent, P., 2008. High-resolution maps of magnetization transfer with inherent correction for RF inhomogeneity and T1 relaxation obtained from 3D FLASH MRI. Magn. Reson. Med. 60 (December(6)), 1396–1407.

Ashburner, J, Ridgway, GR., 2013. Symmetric diffeomorphic modeling of longitudinal structural MRI. Front. Neurosci. 6.
Lorio, S, Fresard, S, Adaszewski, S, Kherif, F, Chowdhury, R, Frackowiak, RS, et al., 2016. New tissue priors for improved automated classification of subcortical brain structures on MRI. NeuroImage 130, 157–166.
Ashburner, J., 2007. A fast diffeomorphic image registration algorithm. NeuroImage 38 (1), 95–113.
Pinheiro, JC, Bates, DM, DebRoy, S, Sarkar, D, 2013. The R development core team. NLME 1–336.
Russell Lenth. emmeans: Estimated Marginal Means, aka Least-Squares Means. 2019;
Tukey, J., 1949. Comparing individual means in the analysis of variance. Biometrics 5 (2), 99–114.
Fox, J., 2015. Applied Regression Analysis and Generalized Linear Models. Sage Publications.
Tabachnick, BG, Fidell, LS, Ullman, JB., 2007. Using Multivariate Statistics, 5. Pearson, Boston, MA.
Fox, J, Friendly, M, Weisberg, S., 2013. Hypothesis tests for multivariate linear models using the car package. R J. 5 (1), 39–52.
Repple, J, Meinert, S, Bollettini, I, Grotegerd, D, Redlich, R, Zaremba, D, et al., 2019. Influence of electroconvulsive therapy on white matter structure in a diffusion tensor imaging study. Psychol. Med..
Jorgensen, A, Magnusson, P, Hanson, LG, Kirkegaard, T, Benveniste, H, Lee, H, et al., 2016. Regional brain volumes, diffusivity, and metabolite changes after electroconvulsive therapy for severe depression. Acta Psychiatr Scand. 133 (2), 154–164.
Kubicki, A, Leaver, AM, Vasavada, M, Njau, S, Wade, B, Joshi, SH, et al., 2019. Variations in hippocampal white matter diffusivity differentiate response to electroconvulsive therapy in major depression. Biol. Psychiatry Cogn. Neurosci. Neuroimaging 4 (3), 300–309.
Lyden, H, Espinoza, RT, Pirnia, T, Clark, K, Joshi, SH, Leaver, AM, et al., 2014. Electroconvulsive therapy mediates neuroplasticity of white matter microstructure in major depression. Transl. Psychiatry 4 (4), e380–e388.
Camilleri, JA, Hoffstaedter, F, Zavorotny, M, Zöllner, R, Wolf, RC, Thomann, P, et al., 2020 1. Electroconvulsive therapy modulates grey matter increase in a hub of an affect processing network. NeuroImage Clin. 25, 102114.
Cano, M, Lee, E, Cardoner, N, Martínez-Zalacaín, I, Pujol, J, Makris, N, et al., 2019. Brain volumetric correlates of right unilateral versus bitemporal electroconvulsive therapy for treatment-resistant depression. J. Neuropsychiatry Clin. Neurosci. 31 (2), 152–158.
Gbyl, K, Videbech, P., 2018. Electroconvulsive therapy increases brain volume in major depression: a systematic review and meta-analysis. Acta Psychiatr Scand. 138 (3), 180–195.
Ota, M, Noda, T, Sato, N, Okazaki, M, Ishikawa, M, Hattori, K, et al., 2015. Effect of electroconvulsive therapy on gray matter volume in major depressive disorder. J. Affect. Disord. 186, 186–191.
Pirnia, T, Joshi, SH, Leaver, AM, Vasavada, M, Njau, S, Woods, RP, et al., 2016. Electroconvulsive therapy and structural neuroplasticity in neocortical, limbic and paralimbic cortex. Transl. Psychiatry 6 (6), e832–e838.
Cano, M, Martínez-Zalacaín, I, Bernabéu-Sanz, Á, Contreras-Rodríguez, O, Hernández-Ribas, R, Via, E, et al., 2017. Brain volumetric and metabolic correlates of electroconvulsive therapy for treatment-resistant depression: a longitudinal neuroimaging study. Transl. Psychiatry 7 (2), e1023 –e1023.
Mulders, PCR, Llera, A, Beckmann, CF, Vandenbulcke, M, Stek, M, Sienaert, P, et al., 2020. Structural changes induced by electroconvulsive therapy are associated with clinical outcome. Brain Stimul. Basic Transl. Clin. Res. Neuromodulation 13 (May 1(3)), 696–704.
Leaver, AM, Espinoza, R, Pirnia, T, Joshi, SH, Woods, RP, Narr, KL., 2015. Modulation of intrinsic brain activity by electroconvulsive therapy in major depression. Biol. Psychiatry Cogn. Neurosci. Neuroimaging 1 (1), 77–86.
Leaver, AM, Vasavada, M, Joshi, SH, Wade, B, Woods, RP, Espinoza, R, et al., 2019. Mechanisms of antidepressant response to electroconvulsive therapy studied with perfusion magnetic resonance imaging. Biol. Psychiatry 85 (6), 466–476.
Chau, DT, Fogelman, P, Nordanskog, P, Drevets, WC, Hamilton, JP., 2017. Distinct neural-functional effects of treatments with selective serotonin reuptake inhibitors, electroconvulsive therapy, and transcranial magnetic stimulation and their relations to regional brain function in major depression: a meta-analysis. Biol. Psychiatry Cogn. Neurosci. Neuroimaging 2 (May 1(4)), 318–326.
Cavanna, AE, Trimble, MR., 2006 Mar. The precuneus: a review of its functional anatomy and behavioural correlates. Brain J. Neurol. 129 (Pt 3), 564–583.
Yrondi, A, Nemmi, F, Billoux, S, Giron, A, Sporer, M, Taib, S, et al., 2019. Significant decrease in hippocampus and amygdala mean diffusivity in treatment resistant depression patients who respond to electroconvulsive therapy. Front. Psychiatry 10, 694.
Rouault, TA., 2013. Iron metabolism in the CNS: implications for neurodegenerative diseases. Nat. Rev. Neurosci. 14 (8), 551–564.
Brett, M, Penny, W, Kiebel, S., 2003. Introduction to random field theory. Hum. Brain Funct. 2.
Kiebel, SJ, Poline, JB, Friston, KJ, Holmes, AP, Worsley, KJ., 1999. Robust smoothness estimation in statistical parametric maps using standardized residuals from the general linear model. NeuroImage 10 (6), 756–766.
Bouckaert, F, De Winter, F-L, Emsell, L, Dols, A, Rhebergen, D, Wampers, M, et al., 2016. Grey matter volume increase following electroconvulsive therapy in patients with late life depression: a longitudinal MRI study. J. Psychiatry Neurosci. JPN 41 (March(2)), 105–114.
Rubin-Falcone, H, Zanderigo, F, Thapa-Chhetry, B, Lan, M, Miller, JM, Sublette, ME, et al., 2018. Pattern recognition of magnetic resonance imaging-based gray matter volume measurements classifies bipolar disorder and major depressive disorder. J. Affect. Disord. 227, 498–505.
Chang, M, Womer, FY, Edmiston, EK, Bai, C, Zhou, Q, Jiang, X, et al., 2018. Neurobiological commonalities and distinctions among three major psychiatric diagnostic categories: a structural MRI study. Schizophr Bull 44 (1), 65–74.
MacMaster, FP, Carrey, N, Langevin, LM, Jaworska, N, Crawford, S., 2014. Disorder-specific volumetric brain difference in adolescent major depressive disorder and bipolar depression. Brain Imaging Behav 8 (1), 119–127.
Niu, M, Wang, Y, Jia, Y, Wang, J, Zhong, S, Lin, J, et al., 2017. Common and specific abnormalities in cortical thickness in patients with major depressive and bipolar disorders. EBioMedicine 16, 162–171.